Combining Ensemble Kalman Filter and Multiresolution Analysis for Efficient Assimilation into Adaptive Mesh Models*

A. Siripatana† L. Giraldi‡ O. P. Le Maître§ O. M. Knio¶ I. Hoteit‖

January 6, 2021

Abstract

A new approach is developed for efficient data assimilation into adaptive mesh models with the ensemble Kalman filter (EnKF). The EnKF is combined with a wavelet-based multi-resolution analysis (MRA) scheme to enable robust and efficient assimilation in the context of reduced-complexity adaptive spatial discretization. The wavelet representation of the solution enables the use of different meshes that are individually adapted to the corresponding members of the EnKF ensemble. The analysis step of the EnKF is then performed by involving coarsening, refinement, and projection operations on its ensemble members. Depending on the choice of these operations, five variants of the MRA-EnKF are introduced, and tested on the one dimensional Burgers equation with periodic boundary condition. The numerical results suggest that, given an appropriate tolerance value for the coarsening operation, four out of the five proposed schemes significantly reduce the computational complexity of the assimilation system, with marginal accuracy loss with respect to the reference, full resolution, EnKF solution. Overall, the proposed framework offers the possibility of capitalizing on the advantages of adaptive mesh techniques, and the flexibility of choosing suitable context-oriented criteria for efficient data assimilation.

Keywords— Ensemble Kalman Filter, Multiresolution Analysis, Adaptive Mesh Model

1 Introduction

Numerical simulations of physical problems are always subjected to uncertainty due to limited knowledge of the systems under consideration [1]. These include the approximation of physics, boundary and initial conditions, model parameters and imperfect discretization schemes [37]. The sensitivity of the model solution to such errors must (generally) be identified, quantified and reduced to improve the model prediction.

Uncertainty propagation/reduction methods based on Bayesian inference are now widely applied to enhance the predictive capability of the geophysical fluid dynamics and hydrological models e.g. [20, 41, 42, 43, 44]. Within the Bayesian framework, uncertainty in model input is represented using random variables with known probability laws. Once data becomes available, this prior knowledge is updated via Bayes rule, which yields a generally correlated posterior with reduced uncertainty. Two popular approaches in Bayesian inversion have been extensively applied by the modeling community. The first approach uses a Markov Chain Monte Carlo (MCMC) method to sample the posterior distribution. MCMC techniques require a large number of model runs in order to generate a large enough sample representing the posterior

*Published in *Computational Geosciences*, **23**:6, pp. 1259–1276, (2019).

†King Abdullah University of Science and Technology, Thuwal, Saudi Arabia. (adil.siripatana@kaust.edu.sa).

‡King Abdullah University of Science and Technology, Thuwal, Saudi Arabia. (loic.giraldi@kaust.edu.sa).

§LIMSI-CNRS, Orsay, France. (olm@limsi.fr).

¶King Abdullah University of Science and Technology, Thuwal, Saudi Arabia. (omar.knio@kaust.edu.sa).

‖King Abdullah University of Science and Technology, Thuwal, Saudi Arabia. (ibrahim.hoteit@kaust.edu.sa).

distribution [18, 24, 39]; this often renders the direct application of MCMC to sample large-scale models a computationally prohibitive exercise. Another popular approach for tackling the Bayesian estimation problem is the filtering method, in which the distribution is updated sequentially as the data become available [46]. Among many Bayesian filters, the most popular filtering approach in the field of geophysical fluid dynamics is the so-called Ensemble Kalman Filter (EnKF) and its variants e.g. [3, 8, 9, 29, 25, 47]. Motivated by a Monte Carlo formulation, EnKFs represent the Bayesian filter statistics through an ensemble of system states. These ensemble members, which represent realizations of the random state, are integrated using the dynamical model to estimate the forecast. Once data become available, a linear Kalman update is applied in the so-called analysis step to update the forecast with the new information. Despite its Gaussian underpinning, one of the main advantages of EnKF methods over MCMC techniques is the ability of the former to accommodate large dimensional state vectors at reasonable computational requirements [2, 12, 27, 28, 26, 33, 40].

In fluid dynamics simulations, the loss of solution accuracy due to limited spatial resolution can constitute a major source of uncertainties. Traditionally, a spatial mesh is used that is *a priori* sufficiently fine to capture underlying large- and small-scale dynamics, at the cost of a heavy computational burden. This motivated the development of adaptive mesh refinement (AMR) methods that allow the mesh to adapt its resolution locally according to the features of the solution [4, 6, 7, 13, 32]. AMR enables the simulated mesh to adapt both in space and time, assigning high spatial resolution to the areas in which the solution varies rapidly, and coarsening the mesh in regions of weaker variability. This makes AMR particularly useful for capturing sharp fronts and shock formations [5, 21]. By limiting the fine resolution to regions where it is required, AMR-based simulations significantly reduce the computational complexity and accordingly enhance the computational performance. AMR approaches can be separated into two main classes. The first AMR class splits computational cells into finer cells on the same grid [10], whereas the second one constructs the adaptive grid over a multi-level mesh structure [7].

Recently, the possibility of performing data assimilation using adaptively discretized models grasped the attention of the ocean and hydrodynamics modeling community [6, 14, 30, 35, 36]. However, the literature dealing with the problem of implementing AMR and data assimilation techniques remains scarce. Variational data assimilation methods such as 3D-VAR and 4D-VAR were applied to adaptive mesh ocean and meteorological models in [16] and [38], respectively. The first attempt to combine a sequential data assimilation method, e.g. the EnKF, with an adaptive ocean model was proposed in [14]. The recent contribution by [30] is the first attempt to investigate the implementation of EnKF with multi-level AMR for data assimilation into large-scale coastal ocean models. To address the difficulties in computing the mean and error covariance required in the analysis step of the EnKF, the updates in [30] were performed by projecting each ensemble member from their own mesh to a "supermesh", which is the union of all the meshes associated with the ensemble members. The combination of Multiresolution Analysis (MRA) [23] with EnKF has also been attempted by [19] and [17] in different a context, specifically focusing on history matching problems. [19] introduces an MRA-based DA framework, based on first performing coarse-scale DA to estimate large-scale features of the field properties, followed by DA at smaller scales to refine initial estimates. [17] explores a similar coarse-scale DA methodology, based on combining MRA with ensemble smoother, and show that it leads to more robust estimates than with standard localization approaches. In [19, 17] MRA is applied to solutions obtained on the same fine grid, and the DA aims at inferring parameter fields. In this contribution, MRA is used as part of discretization, and individual ensemble members live of different grids.

In this paper, new approaches combining an EnKF and adaptive mesh models are proposed and analyzed. We rely on a MRA approach to decompose the model solution into Haar wavelets. A convenient tree structure representation is used for this purpose [49]. Depending on the criterion specified by the user, the leaf nodes of the tree are removed or added to adapt the mesh. We design our combined MRA-EnKF schemes in such a way that the adaptive mesh refinement is integrated with the forecast steps of the EnKF in a straightforward fashion, similar to the multi-level AMR proposed in [30]. By defining different projection spaces in the Kalman update step, several MRA-EnKF variants are derived. To analyze the performance of these alternative schemes, we design a simplified system, namely the one-dimensional Burger's equation

in a periodic domain. This setting enables us to efficiently analyze the behavior of all proposed schemes, and to contrast their performances, both in terms accuracy and computational cost, and consequently assess their relative merit. The gained experiences would enable us to infer the significance of these new schemes in the context of more generalized multi-dimensional settings, as recently performed in [14, 30].

The study is organized as follows. The background of the EnKF and MRA are outlined in Section 2. Section 3 presents in detail the derivation of several MRA-EnKF schemes. The test problem and the numerical scheme of our experimental system are presented in Section 4. The results of the numerical experiments are presented and discussed in Section 5. The main conclusions are summarized in Section 6.

2 Background

2.1 Multiresolution analysis

We consider the following transient hyperbolic partial differential equation on the one-dimensional domain $\Omega = (0, L)$,

$$\partial_t u + \partial_x f(u) = 0, \tag{1}$$
$$u(x, 0) = u_0, \tag{2}$$
$$u(0, t) = u(L, t), \tag{3}$$

where u is a scalar field, u_0 is the initial condition, and $f : \mathbb{R} \to \mathbb{R}$ is the flux function. We consider a regular discretization of the domain into N cells of fixed size h. The boundaries of the cells are denoted $(x_i)_{i=0}^N$, where $x_i = ih$. The equation is spatially discretized using a finite volume scheme, and advanced in time using an explicit time integration scheme with an adaptive time step, λ, that is restricted by the Courant-Friedrichs-Lewy condition. The resulting discrete system of equations is denoted by

$$\boldsymbol{u}^{s+1} = \boldsymbol{u}^s - \lambda^s \left(\boldsymbol{f}^{+,s} - \boldsymbol{f}^{-,s} \right), \tag{4}$$

where $\boldsymbol{u}^s \in \mathbb{R}^N$ is the solution vector, $\boldsymbol{f}^{+,s}$ and $\boldsymbol{f}^{-,s}$ are the numerical fluxes at time $t = t_s$. The solution is represented using the piecewise constant expansion

$$u(x, t_s) \approx \mathrm{U}(x, t_s) = \sum_{i=1}^{N} u_i^s \chi_i(x),$$

where χ_i is the characteristic function of the cell (x_{i-1}, x_i). To simplify the notation, the variable t_s is omitted in the rest of the section.

In order to compress the approximation of u, we introduce a multiresolution analysis method based on the Haar transform. To this end, we consider the mother wavelet function $\psi^0(x)$ and the associated scaling function $\phi^0(x)$ defined by

$$\psi^0(x) = \begin{cases} 1 & \text{for } 0 \leqslant x < \frac{1}{2}, \\ -1 & \text{for } \frac{1}{2} \leqslant x < 1, \\ 0 & \text{otherwise,} \end{cases} \qquad \text{and} \qquad \phi^0(x) = \begin{cases} 1 & \text{for } 0 \leqslant x < 1, \\ 0 & \text{otherwise.} \end{cases}$$

We define a rescaled version of the Haar functions according to:

$$\phi(x) = \frac{1}{L^{\frac{1}{2}}} \phi^0 \left(\frac{x}{L} \right) \qquad \text{and} \qquad \psi_{n,j}(x) = \frac{2^{\frac{n}{2}}}{L^{\frac{1}{2}}} \psi^0 \left(2^n \frac{x}{L} - j \right),$$

where the two integer subscripts n and j indicate the resolution level and the position index of the rescaled Haar functions, respectively. This above family constitutes an orthonormal system with the inner product defined by $\langle v, w \rangle_{L^2} = \int_0^L v(x) w(x) \mathrm{d}x$, where v and w are square-integrable function. An expansion of U can be computed by direct projection, i.e.

$$\mathrm{U}(x) = \langle \mathrm{U}, \phi \rangle_{L^2} \, \phi(x) + \sum_n \sum_j \langle \mathrm{U}, \psi_{n,j} \rangle_{L^2} \, \psi_{n,j}(x).$$

In this work, we restrict ourself to the case $N = 2^{n_0}$, where n_0 is the maximum resolution level. Given the piecewise constant structure of u at each time step, the same wavelet transform of the discrete solution can be efficiently computed using a fast Haar transform [22]. The exact resulting expansion is

$$\mathrm{U}(x) = v_0\phi(x) + \sum_{n=0}^{n_0-1}\sum_{j=0}^{2^n-1} v_{n,j}\psi_{n,j}(x), \tag{5}$$

where v_0 is the so-called average coefficient and $\boldsymbol{v}_n \in \mathbb{R}^{2^n}$ is the vector of detail coefficients at level n. It is convenient to index the details using a binary tree structure $\mathcal{T}_P$ such that:

- the root of the tree is the pair $(0, 0)$,
- a node has two children or none,
- a node without a child is a leaf,
- for each non leaf node (n, j), the left (resp. right) son is $(n + 1, 2j)$ (resp. $(n + 1, 2j + 1)$),
- the maximum height of the tree is n_0.

The subscript P indicates that we are considering the perfect binary tree satisfying the above constraints. We denote by $\mathcal{I}(\mathcal{T}_P)$ the set of interior nodes of the tree and $\mathcal{L}(\mathcal{T}_P)$ the set of leaves. (Note that the basis functions, $\psi_{n,j}$, are indexed in the same fashion as their support). For a node $\alpha = (n, j)$, the support of ψ_α denoted by $\Omega_\alpha = [\frac{L}{2^n}j, \frac{L}{2^n}(j + 1))$, and the support of the function associated to its left and right sons denoted by α_ℓ and α_r, respectively, form a partition of the support of the parent, i.e.

$$\Omega_{\alpha_\ell} \cup \Omega_{\alpha_r} = \Omega_\alpha \quad \text{and} \quad \Omega_{\alpha_\ell} \cap \Omega_{\alpha_r} = \varnothing.$$

The wavelet expansion of U is then written as

$$\mathrm{U}(x) = v_0\phi(x) + \sum_{\alpha\in\mathcal{I}(\mathcal{T}_P)} v_\alpha\psi_\alpha(x),$$

with the sum taken over the interior nodes of the tree.

We introduce a thresholding operator Π_ε that satisfies

$$\|\mathrm{U} - \Pi_\varepsilon(\mathrm{U})\|_{L^2} \leqslant \varepsilon.$$

The operator is defined such that the basis function associated to a node $\alpha = (n, j)$ is discarded if the following three conditions are satisfied:

- the coefficient v_α satisfies
$$|v_\alpha| \leqslant 2^{-\frac{n}{2}} n_0^{-\frac{1}{2}} \varepsilon, \tag{6}$$
- all the nodes of the left and right subtrees of α satisfy condition (6),
- the subtree $\mathcal{T}$ of $\mathcal{T}_P$ associated to $\Pi_\varepsilon(\mathrm{U})$ is graded.

The graded condition means that the ratio of the sizes between two neighboring leaves does not exceed two. A graded tree is such that, for two leaves $\alpha_1 = (n_1, j_1)$ and $\alpha_2 = (n_2, j_2)$ with adjacent associated support Ω_{α_1}, Ω_{α_2}, the difference of depth is smaller than or equal to one. Formally, if there exists $x \in \Omega$ such that $\overline{\Omega}_{\alpha_1} \cap \overline{\Omega}_{\alpha_2} = \{x\}$, then $|n_1 - n_2| \leqslant 1$, where $\overline{\Omega}_\alpha$ is the closure of Ω_α. This condition is naturally extended to the boundary (i.e. in the case $x = 0$ or $x = L$). As a consequence, the function $\Pi_\varepsilon(\mathrm{U})$ can be written as

$$\Pi_\varepsilon(\mathrm{U})(x) = v_0\phi(x) + \sum_{\alpha\in\mathcal{I}(\mathcal{T})} v_\alpha\psi_\alpha(x). \tag{7}$$

We also introduce the refinement operator $\mathcal{R}$ such that, for any function $w \in \mathcal{U}_\mathcal{T}$, $\mathcal{R}(w) = w$ and the leaf node $\alpha \in \mathcal{I}(\mathcal{T})$ is split once if the depth of α is strictly smaller than $n_0 - 1$, and the resulting tree remains graded. An adaptive version of the scheme in Eq (4) can be defined as:

$$\boldsymbol{u}^{s+1} = \Pi_\varepsilon\left(\mathcal{R}(\boldsymbol{u}^s) - \widetilde{\lambda}^s(\widetilde{\boldsymbol{f}}^{+,s} - \widetilde{\boldsymbol{f}}^{-,s})\right),$$

where $\widetilde{\lambda}^s$, $\widetilde{\boldsymbol{f}}^{+,s}$ and $\widetilde{\boldsymbol{f}}^{-,s}$ are extended versions of λ^s, $\boldsymbol{f}^{+,s}$ and $\boldsymbol{f}^{-,s}$ accounting for the anisotropic discretization. In the following, we denote by $\mathcal{U}_{\mathcal{T}}$ the subspace of $L^2(0,L)$ defined by

$$\mathcal{U}_{\mathcal{T}} = \text{span}\{\phi\} + \text{span}\{\psi_\alpha;\ \alpha \in \mathcal{T}\}.$$

Hence, if $\mathcal{T}_0$ is a subtree of $\mathcal{T}_1$, we have $\mathcal{U}_{\mathcal{T}_0} \subset \mathcal{U}_{\mathcal{T}_1}$.

This work focuses on classical MRA approach, because we are dealing with a simple 1D problem that enables us to systematically assess different combined MRA and EnKF approaches. In more complex settings, second-generation wavelets [45] can be applied, which avoid dyadic constructions and can be adapted to irregular subdomains. Generic adaptive methods, in particular those based on hierarchical meshes, may also be considered. Using such discretization methods would, however, require definition of more elaborate MRA-EnKF operators than those introduced in the next section.

2.2 Ensemble Kalman filter

The Kalman filter is a recursive technique to sequentially estimate the state of a linear dynamical system using available measurements. It provides the best unbiased estimates under the assumption that the underlying distributions are Gaussian [31]. We consider here the ensemble Kalman filter that is designed for large scale nonlinear filtering problems and in which the moments of the Gaussian distributions are estimated using a discrete sample. Given a state-space models defined as

$$\begin{aligned}\mathbf{v}^k &= \mathcal{M}(\mathbf{v}^{k-1}) + \boldsymbol{\eta}^k,\\ \mathbf{y}^k &= H^k\mathbf{v}^k + \boldsymbol{\epsilon}^k,\end{aligned}$$

where $\mathcal{M}$ is the dynamical operator describing the time evolution of the state from time step $k-1$ to k, and H^k a linear observation operator.

The term $\mathbf{v}^k$ is a $\mathbb{R}^{\#\mathcal{T}}$-valued random vector representing the state defined by the expansion coefficients $(v_\alpha)_{\alpha\in\mathcal{I}(\mathcal{T})}$ as in Eq. (7), where $\#\mathcal{T}$ denotes the number of internal nodes in $\mathcal{T}$. $\mathbf{y}^k$ is a $\mathbb{R}^m$-valued random observation vector, $\boldsymbol{\eta}^k$ is the model error and $\boldsymbol{\epsilon}^k$ is the observation error. We assume that $\boldsymbol{\eta}^k$ and $\boldsymbol{\epsilon}^k$ are Gaussian with zero mean and covariance matrices Q^k, and R^k, respectively, i.e., $\boldsymbol{\eta}^k \simeq \mathcal{N}(0, Q^k)$ and $\boldsymbol{\epsilon}^k \simeq \mathcal{N}(0, R^k)$. $\mathbf{v}^0$, $\boldsymbol{\eta}^k$ and $\boldsymbol{\epsilon}^k$ are further assumed to be mutually independent. For the sake of simplification, we omit the superscript k in the rest of the section.

Given an ensemble of N_e forecasts defining a matrix $V^f = [\mathbf{v}_q^f]_{q=1}^{N_e} \in \mathbb{R}^{\#\mathcal{T}\times N_e}$ and the realization of the data $\mathbf{y}$, the (stochastic) EnKF [2, 15, 47] updates the forecasts according to:

$$\mathbf{v}_q^a = \mathbf{v}_q^f + CH^T(HCH^T + R)^{-1}(\mathbf{y}_q - H\mathbf{v}_q^f), \tag{8}$$

where $\mathbf{y}_q = \mathbf{y} + \boldsymbol{\epsilon}_q,\ q = 1, ..., N_e$ is a perturbed observation vector, and C is the sample covariance

$$C = \frac{1}{N_e - 1}\sum_{q=1}^{N_e}\left(\mathbf{v}_q^f - \bar{\mathbf{v}}^f\right)\left(\mathbf{v}_q^f - \bar{\mathbf{v}}^f\right)^T,\ \text{with}\quad \bar{\mathbf{v}}^f = \frac{1}{N_e}\sum_{q=1}^{N_e}\mathbf{v}_q^f.$$

We denote by $\mathbf{h}_q$, $\bar{\mathbf{h}}$, C_H and M the quantities defined by

$$\mathbf{h}_q = H\mathbf{v}_q^f,\quad \bar{\mathbf{h}} = \frac{1}{N_e}\sum_{q=1}^{N_e}\mathbf{h}_q,\ \text{and}\ C_H = \frac{1}{N_e - 1}\sum_{q=1}^{N_e}(\mathbf{h}_q - \bar{\mathbf{h}})(\mathbf{h}_q - \bar{\mathbf{h}})^T. \tag{9}$$

Equation (8) can thus be recast as

$$\mathbf{v}_q^a = \mathbf{v}_q^f + \frac{1}{N_e - 1}\sum_{r=1}^{N_e}(\mathbf{v}_r^f - \bar{\mathbf{v}}^f)(\mathbf{h}_r - \bar{\mathbf{h}})^T(C_H + R)^{-1}(\mathbf{y} + \boldsymbol{\epsilon}_q - \mathbf{h}_q).$$

Let G_{qr}, $\bar{G}_q$ and F_{qr} be defined by

$$G_{qr} = \frac{1}{N_e - 1}(\mathbf{h}_r - \bar{\mathbf{h}})^T(C_H + R)^{-1}(\mathbf{y} + \boldsymbol{\eta}_q - \mathbf{h}_q),\quad \bar{G}_q = \frac{1}{N_e}\sum_{r=1}^{N_e}G_{qr},\ \text{and}\ F_{qr} = G_{qr} - \bar{G}_q.$$

One can then show that

$$\mathbf{v}_q^a = \mathbf{v}_q^f + \sum_{r=1}^{N_e} F_{qr}\mathbf{v}_r^f, \tag{10}$$

where the matrix F only depends on the ensemble members through the predicted observations ensemble $(\mathbf{h}_q)_{q=1}^{N_e}$. Moreover, given the linear nature of the update of the members, the functional representation of the members is also updated as

$$\mathrm{U}_q^a(x) = \mathrm{U}_q^f(x) + \sum_{r=1}^{N_e} F_{qr}\mathrm{U}_r^f(x). \tag{11}$$

Hereafter, we refer to the term $\sum_{r=1}^{N_e} F_{qr}\mathrm{U}_r^f(x)$ in Eq. (11) as the 'correction' term. The analyzed ensemble members are then integrated with the model, $\mathcal{M}$, in the forecast step until the next observation become available, a new EnKF update-forecast cycle then begins.

3 MRA-EnKF methods

This section will present the derivation of the EnKF update step for ensemble members defined on different grids. Five MRA-EnKF schemes employing different projection strategies on the grid on which the EnKF update is performed are proposed, namely, union grid (MRAEnKF), mean grid (MSPEnKF), and members grid (CrPEnKF and CnSPEnKF).

3.1 EnKF update in the MRA settings

For a given time t, we denote by $\mathrm{U}_q(x)$ the q^{th} ensemble member, $1 \leqslant q \leqslant N_e$, and by $\mathcal{T}_q$ the tree associated with U_q. Let $\overline{\mathrm{U}}$ be the mean of the ensemble $(\mathrm{U}_q)^{N_e}$, i.e. the best unbiased estimate of the ensemble which are subjected to the Gaussian assumption, and $\overline{\mathcal{T}}$ be the tree associated with $\overline{\mathrm{U}}$. Then $\overline{\mathrm{U}}$ can be written as

$$\overline{\mathrm{U}}(x) = v_0\phi(x) + \sum_{\alpha\in\mathcal{I}(\overline{\mathcal{T}})} v_\alpha\varphi_\alpha(x), \tag{12}$$

where the function spaces of U_q, $\overline{\mathrm{U}}$ and U are related by

$$\mathcal{U}_{\overline{\mathcal{T}}} \subseteq \cup_{q=1}^{N_e}\mathcal{U}_{\mathcal{T}_q} \subseteq \mathcal{U}_{\mathcal{T}_P}.$$

To compute the mean $\overline{\mathrm{U}}$, all ensemble members are projected onto the union subspace $\cup_{q=1}^{N_e}\mathcal{U}_{\mathcal{T}_q}$, on which the average is calculate.

Based on Eq. (11), one can modify the EnKF update step to accommodate the change in the subspace of the ensemble caused by adaptive mesh refinement during the forecast. The general form of the EnKF update with AMR is then written

$$\mathrm{U}_q^a(x) = \mathscr{P}_{\mathcal{U}_{\mathcal{T}_1}}\left[\mathrm{U}_q^f(x) + \mathscr{P}_{\mathcal{U}_{\mathcal{T}_2}}\left(\sum_{r=1}^{N_e} F_{qr}\mathrm{U}_r^f(x)\right)\right], \tag{13}$$

where $\mathscr{P}_{\mathcal{U}_{\mathcal{T}_i}},\ i = 1, 2$ is the L2 projection of a function onto a subspace $\mathcal{U}_{\mathcal{T}_i}$ defined as

$$\mathscr{P}_{\mathcal{U}_{\mathcal{T}_2}}\mathrm{u} = \underset{\mathrm{v}\in\mathcal{U}_{\mathcal{T}_2}}{\arg\min}\|\mathrm{u} - \mathrm{v}\|_{\mathbf{L}_2}.$$

Since u and v can be expressed with Haar wavelets, which constitute an orthogonal basis in L2 space, if $\mathrm{u}(x)$ is such that

$$\mathrm{u}(x) = v_0\phi(x) + \sum_{\alpha\in\mathcal{I}(\mathcal{T}_1)} v_\alpha\varphi_\alpha(x),$$

and $\mathrm{v}(x)$ is such that

$$\mathrm{v}(x) = v_0\phi(x) + \sum_{\alpha\in\mathcal{I}(\mathcal{T}_2)} v_\alpha\varphi_\alpha(x),$$

then the projection of u on $\mathcal{U}_{\mathcal{T}_1}$ is

$$\mathscr{P}_{\mathcal{U}_{\mathcal{T}_1}} \mathrm{u} = v_0\phi(x) + \sum_{\alpha\in\mathcal{I}(\mathcal{T}_1)\cap\mathcal{I}(\mathcal{T}_2)} v_\alpha\varphi_\alpha(x) + \sum_{\alpha\in\mathcal{I}(\mathcal{T}_2)\setminus\mathcal{I}(\mathcal{T}_1)} 0\cdot\varphi_\alpha(x),$$

which is amount to assigning the correct detail coefficients to the correct nodes that are both in $\mathcal{U}_{\mathcal{T}_1}$ and $\mathcal{U}_{\mathcal{T}_2}$, and assigning 0 as the coefficients for the nodes that are in $\mathcal{U}_{\mathcal{T}_2}$ but not in $\mathcal{U}_{\mathcal{T}_1}$.

An EnKF update performed on the finest grid containing all ensemble members corresponds to using the subspaces $\mathcal{U}_{\mathcal{T}_1} = \mathcal{U}_{\mathcal{T}_2} = \mathcal{U}_{\mathcal{T}_F}$ in Eq. (13), and is equivalent to Eq. (11). By introducing a thresholding operator Π_ε and assigning a different function spaces to the $\mathcal{U}_{\mathcal{T}_i}$s, we introduce in the following subsections several variants of adaptive mesh refinement EnKF algorithms based on the definition of the ensemble mean in Eq. (12) and the EnKF update in Eq. (13).

3.2 MRAEnKF

In the standard (non-adaptive mesh) EnKF, the updates are performed on a fixed space because the ensemble members and the filter estimate are defined on the same mesh; the update is thus straightforward. This is not the case for adaptive mesh where each ensemble member independently adapts its own grid, which prevents the computation of the first- and second-order statistical moments required for the EnKF algorithm. It is then natural to seek a common space of all members to apply the EnKF updates.

In the MRAEnKF method, the ensemble members and the members correction terms of the EnKF are projected onto the subspace spaning the union of the grids of all ensemble members. The updates are then performed according to Eq. (11). This corresponds to $\mathcal{U}_{\mathcal{T}_1} = \mathcal{U}_{\mathcal{T}_2} = \cup_{q=1}^{N_e}\mathcal{U}_{\mathcal{T}_q}$ in Eq. (13). Accordingly, $\mathrm{U}_q^a(x)$ is written as

$$\mathrm{U}_q^a(x) = \mathscr{P}_{\cup_{q=1}^{N_e}\mathcal{U}_{\mathcal{T}_q}}\left[\mathrm{U}_q^f(x) + \mathscr{P}_{\cup_{q=1}^{N_e}\mathcal{U}_{\mathcal{T}_q}}\left(\sum_{r=1}^{N_e} F_{qr}\mathrm{U}_r^f(x)\right)\right].$$

We will hereafter refer to the proposed combined multiresolution analysis with EnKF techniques as the "MRA-EnKFs", namely to avoid any confusion with the specific MRAEnKF method described above.

3.3 Forecast Mean Space Projection (FMSP) EnKF

In the limit of large ensemble, the EnKF converges to the Kalman filter (KF) given the Gaussian noise assumptions on the forecast and observation models [11, 34]. The mean estimate of the EnKF also converges to a maximum a posteriori (MAP) estimate of the KF. Even for the case of nonlinear models, it is a common practice to take the ensemble mean as the filter state estimate. Therefore, it is intuitive to consider performing the ensemble projection on the space of the mean $\mathcal{U}_{\overline{\mathcal{T}}}$. As a consequence, we modify the MRAEnKF by carrying out the update of all members in the mean space, using Haar wavelets function representation.

In FMSP, all the members and correction terms are projected on the subspace of the mean forecast before the analysis step. Let $\overline{\mathrm{U}}^f$ be the mean forecast and $\mathcal{U}_{\overline{\mathcal{T}}^f}$ the subspace associated with $\overline{\mathrm{U}}^f$. FMSP is initialized by coarsening the mean of the forecast,

$$\overline{\mathrm{U}}^f = \Pi_\varepsilon\left(\frac{1}{N_e}\sum_{q=1}^{N_e}\mathrm{U}_q^f\right). \tag{14}$$

U_q^f and the correction term $\sum_{q=1}^{N_e} F_{qr}\mathrm{U}_r^f(x)$ are projected onto $\mathcal{U}_{\overline{\mathcal{T}}^f}$ before applying the EnKF update. This corresponds to setting $\mathcal{U}_{\mathcal{T}_1} = \mathcal{U}_{\mathcal{T}_2} = \mathcal{U}_{\overline{\mathcal{T}}^f}$ in Eq. (13), which leads to

$$\mathrm{U}_q^a(x) = \mathscr{P}_{\mathcal{U}_{\overline{\mathcal{T}}^f}}\left[\mathrm{U}_q^f(x) + \mathscr{P}_{\mathcal{U}_{\overline{\mathcal{T}}^f}}\left(\sum_{r=1}^{N_e} F_{qr}\mathrm{U}_r^f(x)\right)\right].$$

Note that the update in FMSP is performed in $\mathcal{U}_{\overline{\mathcal{T}}^f}$, which is a subset of $\cup_{q=1}^{N_e}\mathcal{U}_{\mathcal{T}_q}$. For certain tolerance, ε, the FMSP solution is expected to be less accurate than that of MRAEnKF, as the latter performs the update in the union space of all members. However, less computational complexity is anticipated for FMSP as it involves a smaller number of grid points.

3.4 Analysis Mean Space Projection (AMSP) EnKF

The order in which one applies the projection and the analysis may affect the performance of the MRA-EnKFs. To explore this, we introduce the Analysis Space Projection (AMSP) EnKF, which consists in another variant of mean space projection EnKF derived by rearranging the order of implementing the projection and analysis.

In contrast with the FMSP, the AMSP projects all the members on the subspace of the mean after the analysis step. Let $(\widetilde{\mathrm{U}}_q^a(x))^{N_e}$ be the intermediate analysis ensemble, the filter starts by computing $\widetilde{\mathrm{U}}_q^a(x)$ with MRAEnKF:

$$\widetilde{\mathrm{U}}_q^a(x) = \mathscr{P}_{\cup_{q=1}^{N_e}\mathcal{U}_{\mathcal{T}_q}}\left[\mathrm{U}_q^f(x) + \mathscr{P}_{\cup_{q=1}^{N_e}\mathcal{U}_{\mathcal{T}_q}}\left(\sum_{r=1}^{N_e} F_{qr}\mathrm{U}_r^f(x)\right)\right].$$

Here $\widetilde{\mathrm{U}}_q^a(x)$ is defined on the union subspace $\cup_{q=1}^{N_e}\mathcal{U}_{\mathcal{T}_q}$. Then the coarsened mean of $(\widetilde{\mathrm{U}}_q^a(x))^{N_e}$ is calculated as

$$\overline{\widetilde{\mathrm{U}}^a} = \Pi_\varepsilon\left(\frac{1}{N_e}\sum_{q=1}^{N_e}\widetilde{\mathrm{U}}_q^a\right).$$

The final analysis $(\mathrm{U}_q^a(x))^{N_e}$ is obtained by projecting $(\widetilde{\mathrm{U}}_q^a(x))^{N_e}$ onto $\mathcal{U}_{\overline{\mathcal{T}}^a}$, namely according to:

$$\mathrm{U}_q^a(x) = \mathrm{P}_{\mathcal{U}_{\overline{\mathcal{T}}^a}}\left[\widetilde{\mathrm{U}}_q^a(x)\right],$$

where $\mathcal{U}_{\overline{\mathcal{T}}^a}$ is the subspace associated with $\overline{\widetilde{\mathrm{U}}^a}$.

3.5 Correction Projection (CrP) EnKF

FMSP and AMSP updates result in all members belonging to the space of the mean. All members are then integrated with the model in the forecast step starting from the same mesh. This may result in each member losing some of its details as possessed prior to the EnKF update. Projecting each member onto its own space before forecasting with the model may enhance the filter performance. Therefore, we also consider projecting each member back to its original space after the EnKF update.

In Correction Projection (CrP) EnKF, all the member corrections are projected on the mean before the analysis step. Each member is then updated in the mean space $\mathcal{U}_{\overline{\mathcal{T}}}^f$ as computed in FMSP (i.e. Eq. (14)), and the members are finally projected back to each member's original subspace $\mathcal{U}_{\mathcal{T}_q}$. Each member is then propagated forward to the next assimilation step. This corresponds to setting $\mathcal{U}_{\mathcal{T}_1} = \mathcal{U}_{\mathcal{T}_q}$ and $\mathcal{U}_{\mathcal{T}_2} = \mathcal{U}_{\overline{\mathcal{T}}^f}$ in Eq. (13). Since the CrP update is performed on the coarse mean subspace, considerable reduction in computational cost can be achieved with respect to EnKF.

3.6 Constant Space Projection (CnSP) EnKF

In Constant Space Projection (CnSP) EnKF, the forecast and the update of each member are performed entirely on its own mesh. No coarsening is involved in the scheme. This requires projecting the correction term onto subspace $\mathcal{U}_{\mathcal{T}_q}$, not $\mathcal{U}_{\overline{\mathcal{T}}}^f$ or $\mathcal{U}_{\overline{\mathcal{T}}}^a$. The update step of CnSP therefore corresponds to setting $\mathcal{U}_{\mathcal{T}_1} = \mathcal{U}_{\mathcal{T}_2} = \mathcal{U}_{\mathcal{T}_q}$ in Eq. (13). Because each member is updated independently in its own space without gaining any extra mesh details from other members, we expect the CnSP to produce less accurate estimates compared to the other methods as time evolves.

Table 1 summarizes the update algorithms of the EnKF and its multiresolution variants. The differences between these schemes arise from the order of application of the update and the coarsening steps. They also depend on the spaces of ensemble members projection.

Method	Algorithm
EnKF	$\mathcal{U}_{\mathcal{T}_1} = \mathcal{U}_{\mathcal{T}_2} = \mathcal{U}_{\mathcal{T}_P}$.
MRAEnKF	$\mathcal{U}_{\mathcal{T}_1} = \mathcal{U}_{\mathcal{T}_2} = \cup_{q=1}^{N_e} \mathcal{U}_{\mathcal{T}_q}$.
FMSP	1. $\overline{\mathrm{U}}^f = \Pi_\varepsilon(\frac{1}{N_e} \sum_{q=1}^{N_e} \mathrm{U}_q^f)$. 2. Obtain $\mathcal{U}_{\overline{\mathcal{T}}^f}$. 3. $\mathcal{U}_{\mathcal{T}_1} = \mathcal{U}_{\overline{\mathcal{T}}^f}$ and $\mathcal{U}_{\mathcal{T}_2} = \mathcal{U}_{\overline{\mathcal{T}}^f}$.
AMSP	1. Compute $(\widetilde{\mathrm{U}}_q^a)^{N_e}$ with MRAEnKF 2. $\overline{\widetilde{\mathrm{U}}^a} = \Pi_\varepsilon(\frac{1}{N_e} \sum_{q=1}^{Q} \widetilde{\mathrm{U}}_q^a)$. 3. Obtain $\mathcal{U}_{\overline{\mathcal{T}}^a}$. 4. $\mathcal{U}_{\mathcal{T}_1} = \mathcal{U}_{\overline{\mathcal{T}}^a}$ and $\mathcal{U}_{\mathcal{T}_2} = \cup_{q=1}^{N_e} \mathcal{U}_{\mathcal{T}_q}$.
CrP	1. Compute $\mathcal{U}_{\overline{\mathcal{T}}^f}$ (See FMSP). 2. $\mathcal{U}_{\mathcal{T}_1} = \mathcal{U}_{\mathcal{T}_q}$ and $\mathcal{U}_{\mathcal{T}_2} = \mathcal{U}_{\overline{\mathcal{T}}^f}$.
CnSP	$\mathcal{U}_{\mathcal{T}_1} = \mathcal{U}_{\mathcal{T}_2} = \mathcal{U}_{\mathcal{T}_q}$.

Table 1: Summary of EnKF and its multiresolution variants.

4 Computational test problem

4.1 Model

We focus on the one-dimensional Burger's equation with periodic boundary conditions, i.e. Eq. (1) with the flux defined as

$$f(u) = u^2/2.$$

In the numerical experiments, the uncertain initial condition corresponds to the shifted Gaussian:

$$u(x, t_0) = b + a \cdot e^{-(x-\mu)^2/\rho^2}, \tag{15}$$

where $b \sim \mathscr{U}(0.5, 1)$, $a \sim \mathscr{U}(1, 3)$, $\mu \sim \mathscr{U}(1, 4)$ and $\rho \sim \mathscr{U}(0.1, 0.5)$. The size of the domain is equal to 4π. Observe that for deterministic a, μ and ρ, the solution $u(x, t > t_0)$ can be recast as $b + u'(x - b \times t, t)$ where u' is deterministic and solves Eq. (1) with the initial data $u'(x, t_0) = a \cdot e^{-(x-\mu)^2/\rho^2}$. In this case, all realizations of $u - b$ are equal up to a translation of $b \times t$ (which has the same distribution as b). However, because of additional uncertainties in the definition of the initial condition, the non-linearity of the Burgers equation prevents us from deriving a simple expression of the solution, in particular for the dynamics after the shock has formed.

4.2 Roe flux calculation

According to Eq. (4), the solution at the i^{th} cell is advanced as:

$$u_i^{s+1} = u_i^s - \lambda^s \left(f_i^{+,s} - f_i^{-,s} \right), \tag{16}$$

where $f_i^{+,s}$ and $f_i^{-,s}$ are the corresponding right and left numerical fluxes, respectively. In the case of a fine mesh, the domain is discretized into 2^{n_0} elements of equal size, where n_0 represents

the maximum depth of the multiresolution representation. In the experiments, the maximum depth is 10; therefore the fine mesh has 1024 cells.

As mentioned earlier, the solution is advanced using an adaptive explicit time integration scheme. Specifically, the time step, λ^s, is adjusted according to $\lambda^s = \text{CFL} \times h/\Lambda$, where Λ is the maximum absolute value of u^s and CFL is a user-defined positive value $\leqslant 1$.

The Burgers equation can develop shocks, and it is essential to use an appropriate definition of the numerical fluxes in Eq.(16) such that it does not create spurious waves. This point is crucial here as we want to make sure that the EnKF algorithms governing the evolution of the ensemble are not plagued by features artificially introduced by the solver used to advance the members in time. Many different approaches are available for the resolution of the Burger equation (*e.g.* ENO, WENO, TVD schemes, flux limiters,...) mostly differing by the defining of the numerical fluxes. In the present work, we decided to rely on one of the simplest definition, the Roe flux [48].

Let us denote $\hat{u} \doteq (u_l + u_r)/2$ the Roe state, and $\triangle u \doteq u_r - u_l$ the state jump. The classical Roe flux is

$$F(u_l, u_r) = \frac{[f(u_l) + f(u_r)]}{2} - \frac{|\hat{u}|}{2} \triangle u.$$

To prevent the Roe flux from violating the entropy condition, the entropy fix is applied, which consists in insuring sufficient diffusion in rarefaction problem with $u_l < 0 < u_r$. Let

$$\delta = \max\{0, \hat{u} - u_l, u_r - \hat{u}\},$$

and define

$$\hat{q} = \begin{cases} \hat{u}, & |\hat{u}| \geqslant \delta \\ \dfrac{\hat{u}^2}{2\delta} + \delta/2, & |\hat{u}| < \delta. \end{cases}$$

The fixed Roe flux is

$$F(u_l, u_r) = \frac{[f(u_l) + f(u_r)]}{2} - \frac{|\hat{q}|}{2} \triangle u,$$

and the right and left fluxes in Eq. (16) are defined through $f_i^{+,s} = F(u_i^s, u_{i+1}^s)$ and $f_i^{-,s} = F(u_{i-1}^s, u_i^s)$, respectively. Note that, here, $u_l = u_i^s$ and $u_r = u_{i+1}^s$ for $f_i^{+,s}$, and $u_l = u_{i-1}^s$ and $u_r = u_i^s$ for $f_i^{-,s}$. Furthermore, because periodic boundary conditions are used, $f_N^{+,s} = f_1^{-,s} = F(u_N^s, u_1^s)$, where N is the number of cells in the domain.

4.3 Multiresolution Roe solver

Given a sequence of N values on the fine grid $\boldsymbol{u} = \{u_j\}_{i=1}^N$, [23] showed that there is a one-to-one transformation between $\boldsymbol{u}$ and its multiresolution representation, U. The transformation can be expressed as:

$$\mathrm{U} = \mathbf{M}\boldsymbol{u}, \tag{17}$$

where $\mathbf{M}$ depends on the interpolation method implemented by the multiresolution analysis scheme. In this work, the central interpolation is used, and therefore $\mathbf{M}$ is a linear operator expressed by an $N \times N$ matrix.

We can symbolically recast Eq. (4) in the form of cell-wise update on the finest grid according to

$$u_i^{s+1} = u_i^s - \lambda^s \left(f_i^{+,s} - f_i^{-,s}\right) \equiv (\mathbf{E} \cdot u^s)_i, \quad 1 \leqslant i \leqslant N, \tag{18}$$

where $\mathbf{E}$ is a nonlinear operator representing the action of the explicit update. The multiresolution scheme is obtained by applying $\mathbf{M}$ to Eq. (18), resulting in:

$$\mathrm{U}^{s+1} = \mathrm{U}^s - \lambda^s \mathbf{M}\left(\boldsymbol{f}^{+,s} - \boldsymbol{f}^{-,s}\right) = \mathbf{M}\mathbf{E} \cdot (\mathbf{M}^{-1}\mathrm{U}^s) \equiv \mathbf{E}_M \cdot \mathrm{U}^s. \tag{19}$$

Here $\mathbf{E}_M$ is a multiresolution version of the nonlinear operator $\mathbf{E}$. The thresholding operator can be introduced at the beginning of each time step to incorporate the compression of the numerical solution, which leads to:

$$\mathbf{M}\mathbf{E} \cdot (\mathbf{M}^{-1}\Pi_\varepsilon(\mathrm{U}^s)) \equiv \mathbf{E}_M^\varepsilon \cdot \mathrm{U}^s. \tag{20}$$

It can be shown that [23], given an appropriate tolerance value and a monotone scheme $\mathbf{E}$, the error between the compressed and the full model solution is of the same order of magnitude as the tolerance, which can be written as

$$\| \mathbf{E}_M^{\varepsilon} \cdot \mathrm{U}^s - \mathbf{E}_M \cdot \mathrm{U}^s \|_1 \leqslant \varepsilon, \tag{21}$$

where $\| \mathbf{x} \|_1$ is the L_1 norm of the vector $\mathbf{x}$.

Given the thresholding parameter ε and the resolution level n_0, the algorithm starts by constructing a tree $\mathcal{T}^0$ and the subspace $\mathcal{U}^0$, which are used to represent the cell average initial condition. After the discrete solution is initialized, it is evolved in time following an iterative process. This consists of five main steps: a refinement of the tree $\mathcal{T}$ at the beginning of every time step, the evaluation of $\mathcal{U}$ at the centers of the cells, the computation of the time step satisfying the CFL condition, a time advance of the solution, and finally projection and coarsening. We summarize the multiresolution-based Roe solver as follows.

Steps I. and II. The approximation space is refined in anticipation of additional steepening that may develop in the solution. For this purpose, the grid is refined to add one more level of resolution. Specifically, the tree leaves are refined according to the enrichment strategy presented in [49]. After the fine grid is obtained, the solution is evaluated at the centers of the cells.

Step III. The optimal time step for solution update is computed based on the prescribed CFL limit.

Step IV. In this step, the model integration from time t_s to t_{s+1} is performed. The solution in an individual cell is updated by integration of the Roe fluxes through the cell's boundary as in Eq. (16).

Step V. After the time integration, the Haar transform is used to recover the multiresolution representation of the solution. Then the coarsening operator Π_{ε} described in Section 2.1 is applied. This step defines the details of the tree and provides a compressed solution for the next iteration.

5 Numerical experiments

In this Section, we assess the performance of the proposed MRA-EnKF schemes in term of estimation error and complexity with respect to both a reference solution and the EnKF solution.

5.1 Twin experiments

A twin experiment is designed to assess the performance of the proposed assimilation schemes against the EnKF, based on their efficiency to estimate the reference solution. The reference solution is computed by solving the Burgers equation with an initial condition generated by sampling the parameters in Eq. (15). From the reference solution, we extract the data at locations $x = 4$, 5.5, 7, 8.5, 10 and 11.5, respectively. The data are collected at regular time intervals corresponding to the assimilation frequency of the EnKF schemes, i.e. every second. These data are perturbed with measurement noise $\boldsymbol{\epsilon}_k \simeq \mathcal{N}(0, R = \sigma^2 \mathrm{I})$, with $\sigma^2 = 0.09$ and I the identity matrix. The initial ensembles of the EnKF and MRA-EnKFs are generated by sampling the parameters in Eq. (15) from the same set of priors used to generate the initial condition of the reference solution. In each set of assimilation experiments, all filters are initialized from the same ensemble, and assimilate the same observations. We also perform the experiments with varying ensemble size and tolerance to holistically examine the behavior of the proposed MRA-EnKFs framework.

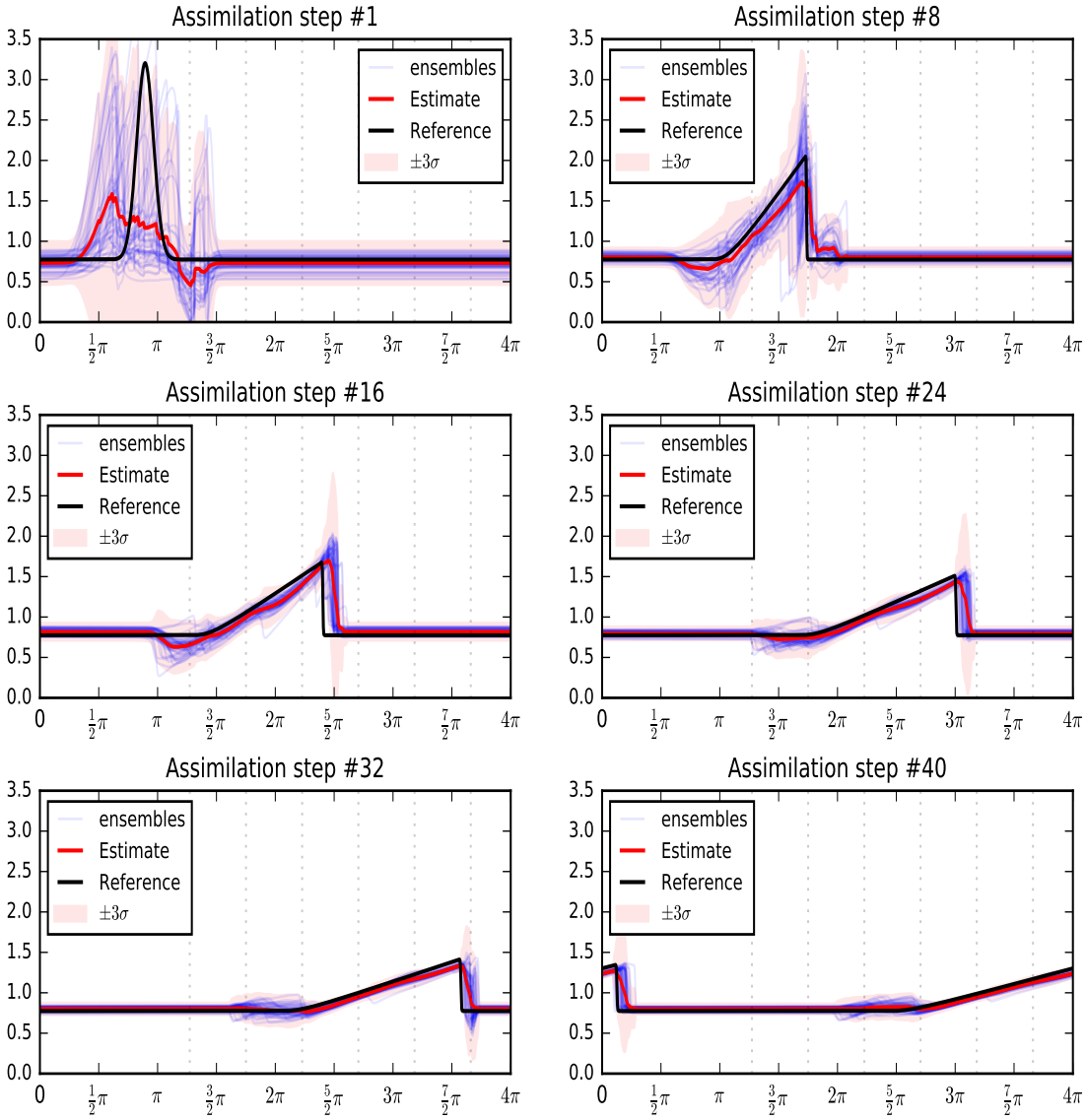

Figure 1: Reference solution vs EnKF solution.

5.2 MRA-EnKFs vs. Reference

In the first experiment, the settings for the multiresolution Roe solver are $\varepsilon = 10^{-3}$, $N_0 = 1024$, and $CFL = 0.9$. We run the simulation for 1 unit of time with 40 assimilation steps (one assimilation every 0.025 unit of time). Figure 1 illustrates the result of a fine grid approximation of the Burger's equation solution. Both the reference solution and the EnKF estimate with similar find grid resolution are shown. The initial condition of the reference solution and of the ensemble members are illustrated in the first subplot of Figure 1. The following subplots depict the evolution of the system at different times. The black solid line is the reference solution at a fixed time step and the red solid line is its EnKF estimate. A total of 48 ensemble members are used for the EnKF. The evolution of the ensemble members is plotted along with the 3 standard deviation bounds to represent the ensemble spread. The ensemble members are marked with the blue lines and the 3 standard deviation bounds around the mean are highlighted in transparent blue. As time evolves, the solution develops a shock between $x = \frac{3}{2}\pi$ and $x = 2\pi$ at $t = 0.2$ (8^{th} assimilation iteration). This discontinuity in the form of a shock is the result of the compressibility due to different wave speed at different points when the hyperbolic PDEs are

solved [23]. This shock formation is well captured by the Roe scheme. It is also clear from the figures that, as the assimilation cycle advances, the ensembles spread around the mean decreases and all members move closer to the reference solution. The filter well maintains the spread around the shock formation.

Initially, the estimate is far from the reference solution. As time evolves, the members start to converge toward the truth. The shock pattern is also well recovered by the EnKF. However, at the 16^{th} assimilation step, we observe the phase shift of the shock: the shock pattern estimated by the EnKF has slightly preceded the reference solution. This is because, at the initial time step, some ensemble members are shifted to the front with respect to the reference initial function. EnKF hardly recovers the head and the tail of the shock due to large ensemble variance at these locations.

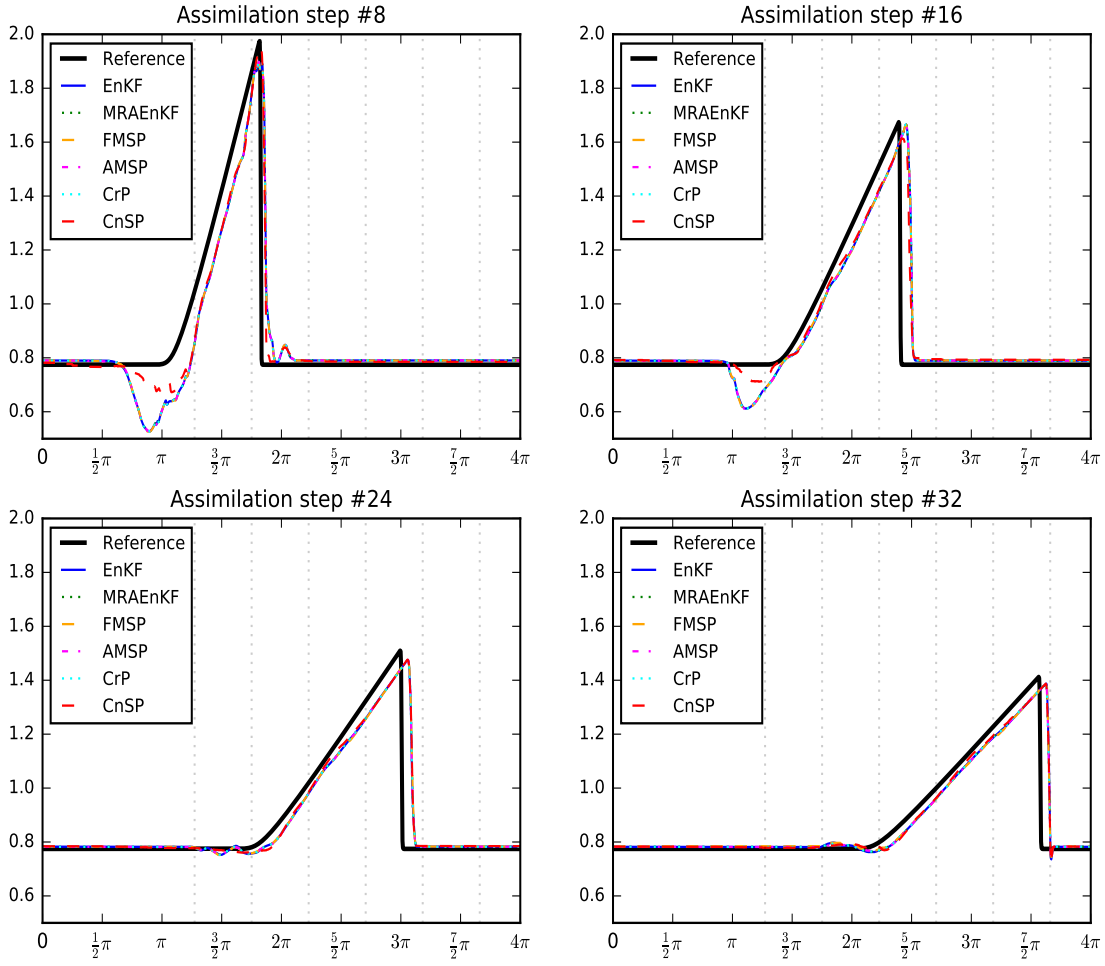

Figure 2: Reference vs. MRA-EnKFs (ensemble mean estimates).

The time evolution of MRA-EnKFs estimates are plotted together with the EnKF and the reference solutions in Figure 2. With a sufficiently large maximum level of the tree, n_0, and ensemble size (48 members), all MRA-EnKFs solutions converge to the reference as the assimilation advances. Most MRA schemes appear to perform as good as EnKF in term of accuracy of the estimates, except CnSP which slightly deviates away from the rest, depicted by the dashed red plot around the tail of the shock formation in the 8^{th} assimilation step of Figure 2. This is because whereas other MRA-EnKFs rely on the union space for the updates, CnSP performs the model integration and the update purely in the space of the members, which may result in loss of solution details.

5.3 Assessment of MRA-EnKFs performances

Two main criteria are used to evaluate the efficiency of a MRA-EnKF; estimation accuracy and computational complexity. The MRA-EnKFs results are evaluated against that of the EnKF, which is taken as the reference. This is justified because the EnKF is always performed on the fine mesh, and thus is considered to be the most accurate filter. An MRA-EnKF scheme is considered efficient if its estimation error is close to that of EnKF and its computational complexity is significantly less than that of the EnKF. A number of factors, such as the ensemble size and the value of thresholding parameter (the tolerance) play an important role in evaluating the overall performance of the MRA-EnKF schemes.

5.3.1 MRA-EnKFs convergence analysis

We first consider the time evolution of the normalized L2 error to examine the convergence of MRA-EnKFs estimates toward the EnKF estimate defined as

$$\text{L2-error} = \frac{\mathbb{E}\left(\int_\Omega \left(u(x) - u^{\text{EnKF}}(x)\right)^2 \mathrm{d}x\right)^{\frac{1}{2}}}{\|u\|_{L_2}},$$

where u^{EnKF} denotes the EnKF solution and $\|u\|_{L_2}$ denotes the L2 norm of u.

Figure 3 plots the time evolution of the normalized L2 error in log scale for each of the MRA-EnKF schemes. The x-axis is the assimilation time step and the y-axis is the average L2 error in log scale. The plotted errors are averages over five assimilation runs with different initial ensembles. The results are consistent with those of Figure 2 with CnSP producing the largest discrepancy from the EnKF. As time advances, the L2 error produced by CnSP is clearly larger than that of the other schemes. The overall decreasing L2 error trends over time indicate the relevance of the MRA-EnKFs for approximating the EnKF solution.

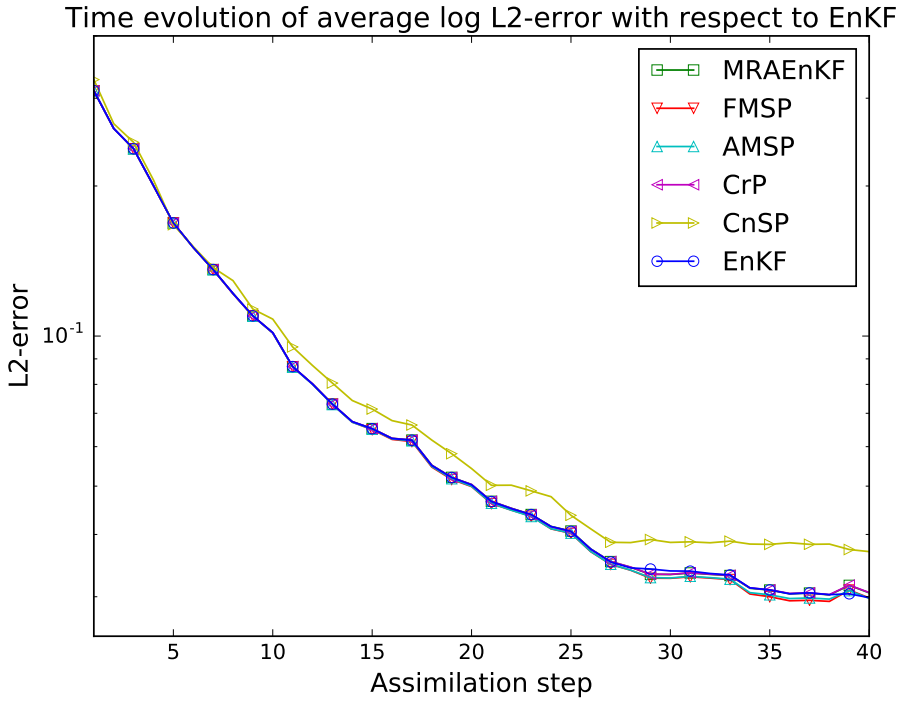

Figure 3: Normalized L2 error versus assimilation step.

We also examine the differences between the MRA-EnKF estimates and the EnKF estimate as the root of the square of the differences of MRA-EnKF and EnKF solutions. Figure 4 shows the

time evolution of the RMSE for each MRA-EnKF scheme. The x-axis is the assimilation step and the y-axis is the RMSE in log scale. Clearly, for this particular tolerance ($\varepsilon = 10^{-3}$), MRAEnKF leads to the smallest error at every assimilation cycle. This is expected because the updates are performed in the members union space with high mesh resolution. The RMSE gradually increases with time for all MRA-EnKF schemes, except CnSP which shows a RMSE decrease after starting from a large error before it increases again toward the end of the assimilation window.

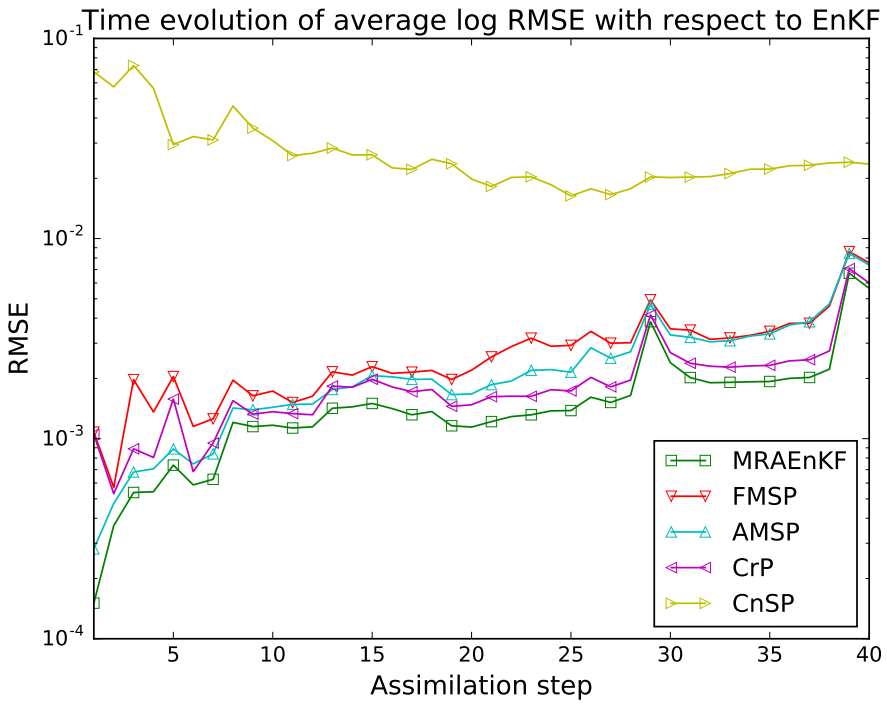

Figure 4: RMSE versus assimilation step.

To investigate the sensitivity of the MRA-EnKFs solutions to a change in the tolerance value, the twin experiment was repeated with different values of ε. Figure 5 plots the time evolution of RMSEs with varying tolerance values ranging from 10^{-3} to 3×10^{-1}. For all schemes, larger tolerance results in larger errors, as expected, as these lead to coarser meshes. With the exception of CnSP, the same RMSE evolution trend is observed for all schemes, with the RMSE gradually increasing and leveling off at the later timesteps for all tolerances.

5.3.2 Estimation error vs. Computational complexity

The computational complexity of data assimilation with an adaptive mesh model is estimated based on the number of the Roe flux computations, which depends on the number of cells used to approximate the solution. Adapting the mesh of each member independently may significantly reduce the model integration cost in the forecast step. Previously, we demonstrated that, given a specific tolerance, the first four MRA-EnKF schemes show no significant differences in terms of estimation error. In this subsection, we simultaneously analyse the estimation error and computational complexity of the MRA-EnKF schemes.

Figure 6 plots the time-integrated RMSE and computational complexity of each MRA-EnKF scheme for varying tolerance and ensemble size. Each subplot representing individual scheme shows normalized complexity on the x-axis against time-integrated RMSE in log scale on the y-axis. We define time-integrated RMSE as the total sum of the RMSE over all assimilation steps. The normalized complexity is defined as a ratio between the number of computed fluxes of the MRA-EnKF scheme and the number of computed fluxes in the EnKF (which runs on the fine mesh). Each curve of the plots represents a given ensemble size but varying tolerance.

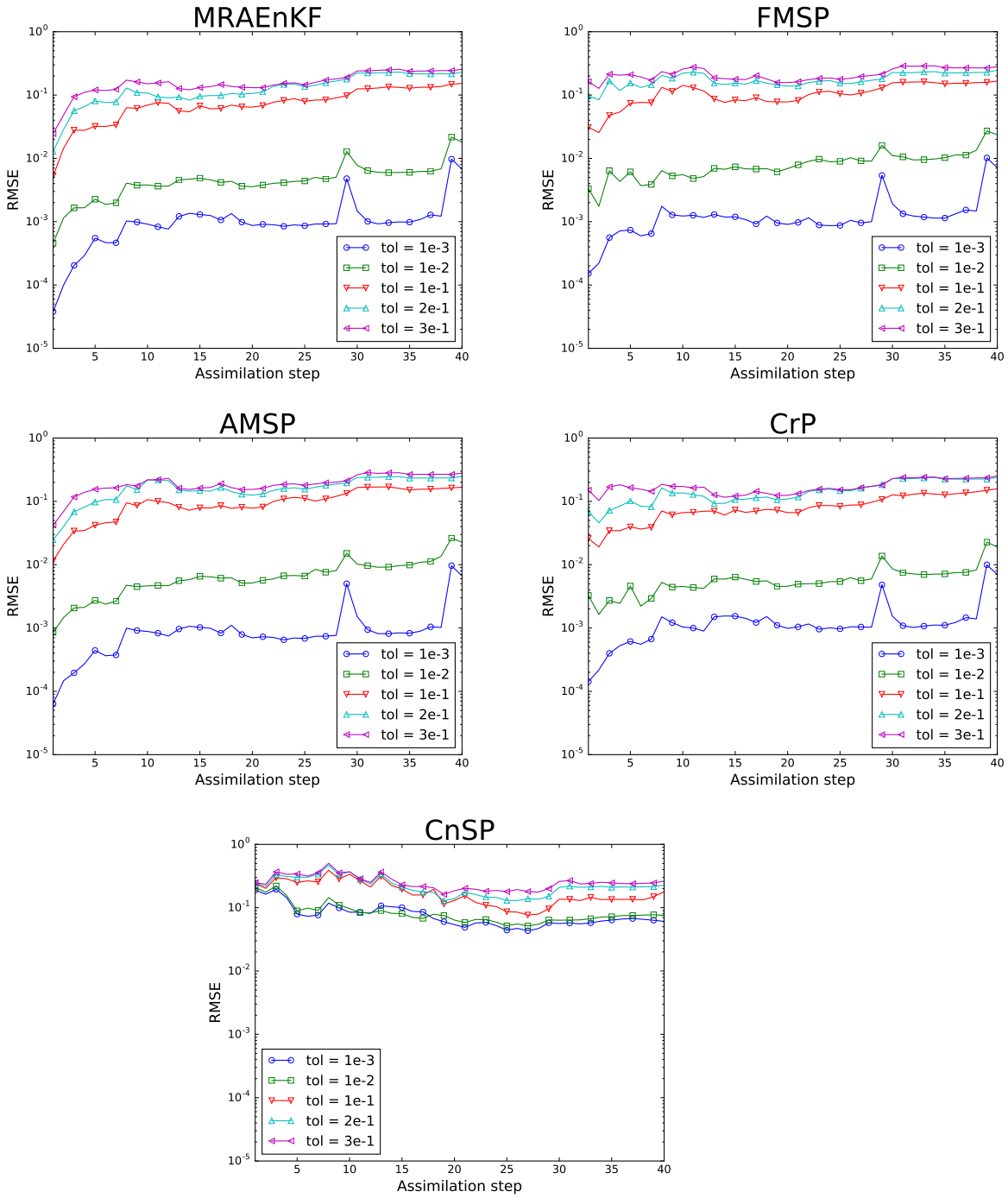

Figure 5: RMSE versus assimilation step. For each scheme, curves are generated for different tolerances, as indicated.

The first observation we make from Figure 6 is that, with the exception of CnSP, as we increase the computational complexity by decreasing the value of the tolerance, the error decreases for all schemes and for all ensemble sizes. This is because a smaller tolerance yields higher mesh resolution, and hence more accurate estimates. The second observation is that for all schemes, increasing the ensemble size beyond $N_e = 16$ does not significantly improve the accuracy of the estimates. This suggests that for a sufficiently large ensemble, the filtering error is dominated by mesh resolution (coarsening). The third observation is that, except for CnSP, large drops in the error occur between the normalized complexity of 0.4 and 0.6. This indicates a range with in which the trade-off between error and complexity is optimal, which provides the best performance of MRA-EnKF schemes, in term of both estimation error and computational cost. Except for CnSP, all MRA-EnKF schemes successfully reduce the computational complexity up to 40%, with an almost negligible time-integrated RMSE of less than $\mathcal{O}(10^{-10})$ when a small tolerance ($\varepsilon = 10^{-10}$) is used.

The above results suggest that, for a specific scheme, increasing the ensemble size beyond some threshold does not improve the filter's performance. However, for a specific ensemble size, the schemes may exhibit different behaviors. We compare the error and complexity of the MRA-EnKFs in Figure 7. The first four MRA-EnKF schemes produce approximately the same error-complexity plots with small ensembles ($N_e \leqslant 16$). This indicates that for small N_e, the error in the assimilation system is dominated by ensemble sampling errors, and not by grid coarsening. For larger ensembles ($N_e > 16$), the error-complexity plots become more distinct. First, for $N_e = 24$, with the normalized complexity of 0.57, FMSP produces almost two orders of magnitude larger error than the other schemes, except CnSP. This result suggests that for a specific ensemble size and tolerance, some schemes may perform better than the others in reducing the estimation error. Similar conclusions can be made for larger ensembles ($N_e > 24$); with the exception of CnSP, FMSP yields slightly larger error than the other schemes within the 0.4-0.6 normalized complexity interval. The MRAEnKF provides the lowest error for any ensemble size and tolerance, which is expected given that MRAEnKF performs the analysis on the union space that yields very high mesh resolution compared to the other schemes. As we increase the ensemble size to 96 members, the differences between the different filtering schemes in term of error become clear. MRAEnKF and CrP yield approximately the same smallest error for all tolerances. This suggests that by projecting each member back to its original subspace before proceeding with the forecast step, CrP greatly improves the filter performance compared to the other schemes. Nevertheless, the results in Figure 7 suggest that, given the same tolerance, the computational complexity of the first four schemes are quite similar regardless of the ensemble size.

We also directly investigated the effect of the change in the error to the change in the tolerance. In Figure 8, the errors are plotted against the tolerance used in the MRA-EnKF schemes. Each curve represents the RMSE for a single ensemble size and varying tolerances. Similar to our previous observations, these plots suggest that for all tolerances, increasing the ensemble beyond a certain size does not significantly improve the performances of these schemes in term of estimation error. Particularly for large tolerances, using large ensembles has a small impact on the filters results. With the exception of CnSP, the linear trend of the error versus tolerance plots is clear. For some tolerance interval (10^{-10} to 10^{-2}), the RMSE is approximately of the same order of magnitude as the tolerance. This is consistent with the inequality in Eq.(21), which shows that the error between the numerical solution and its coarsened multiresolution counterpart is bounded by the tolerance.

Overall, with the exception of CnSP, the results suggest that all schemes are comparatively efficient at approximating the EnKF solution computed on the fine gird. These effectively capture the details of the reference solution given appropriate tolerances, and are all competitive in term of reducing the computational complexity. These schemes demonstrate the ability to significantly reduce the computational complexity by half while providing a RMSE comparable to that of the EnKF.

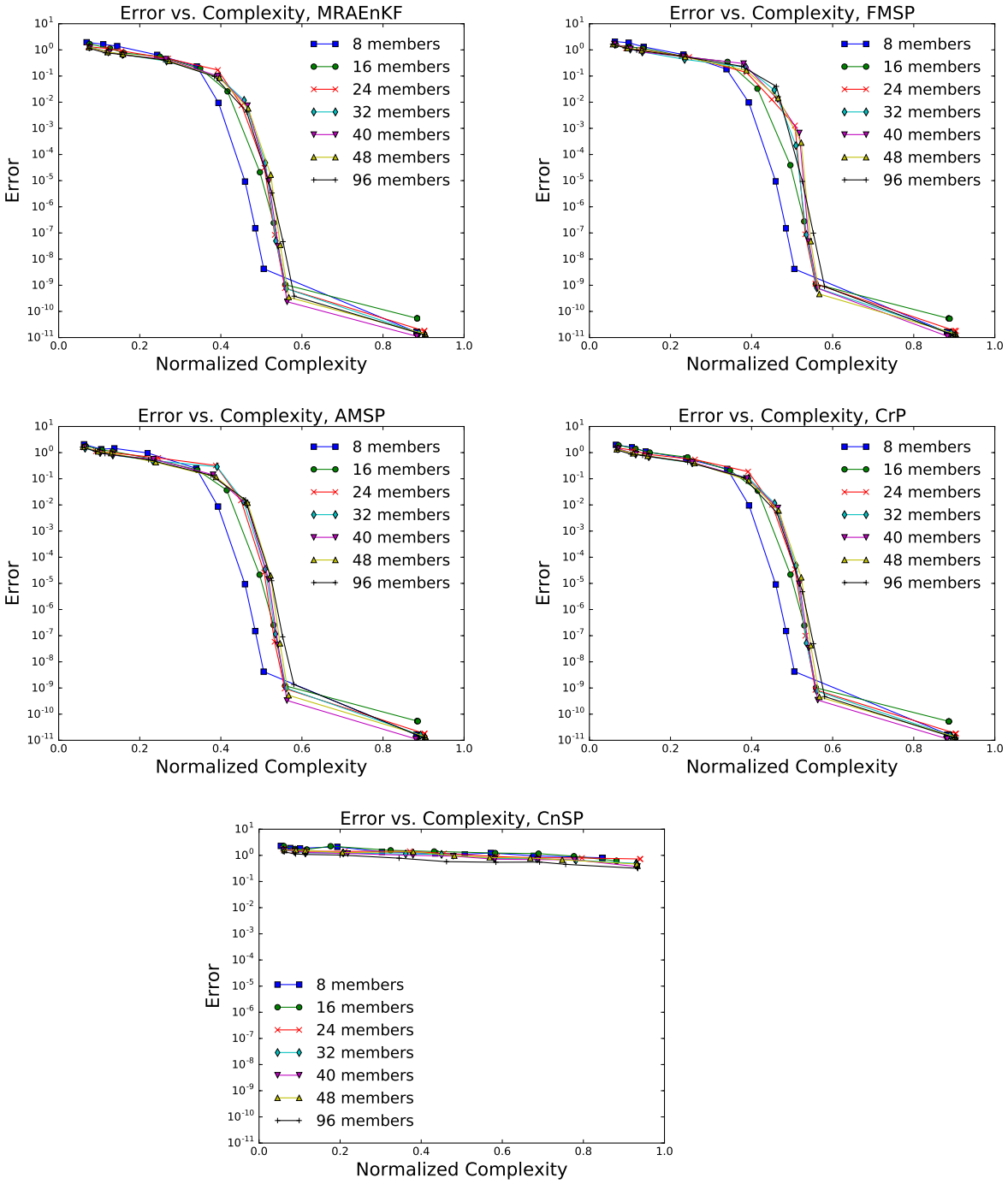

Figure 6: time-integrated RMSE versus normalized complexity. For each scheme, curves are generated for different ensemble size, as indicated.

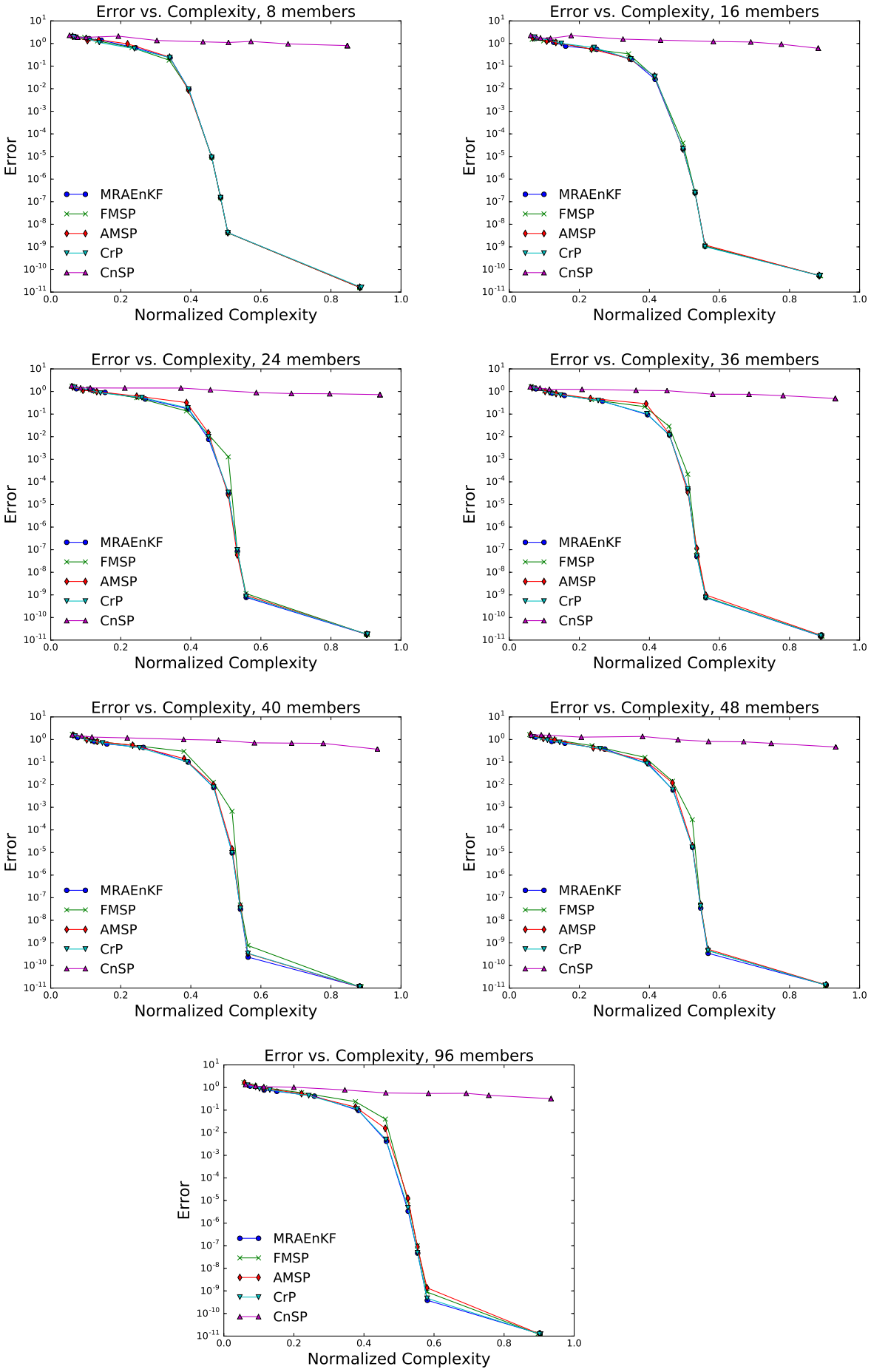

Figure 7: time-integrated RMSE versus normalized complexity. For each ensemble size, curves are generated for different MRA-EnKF scheme, as indicated.

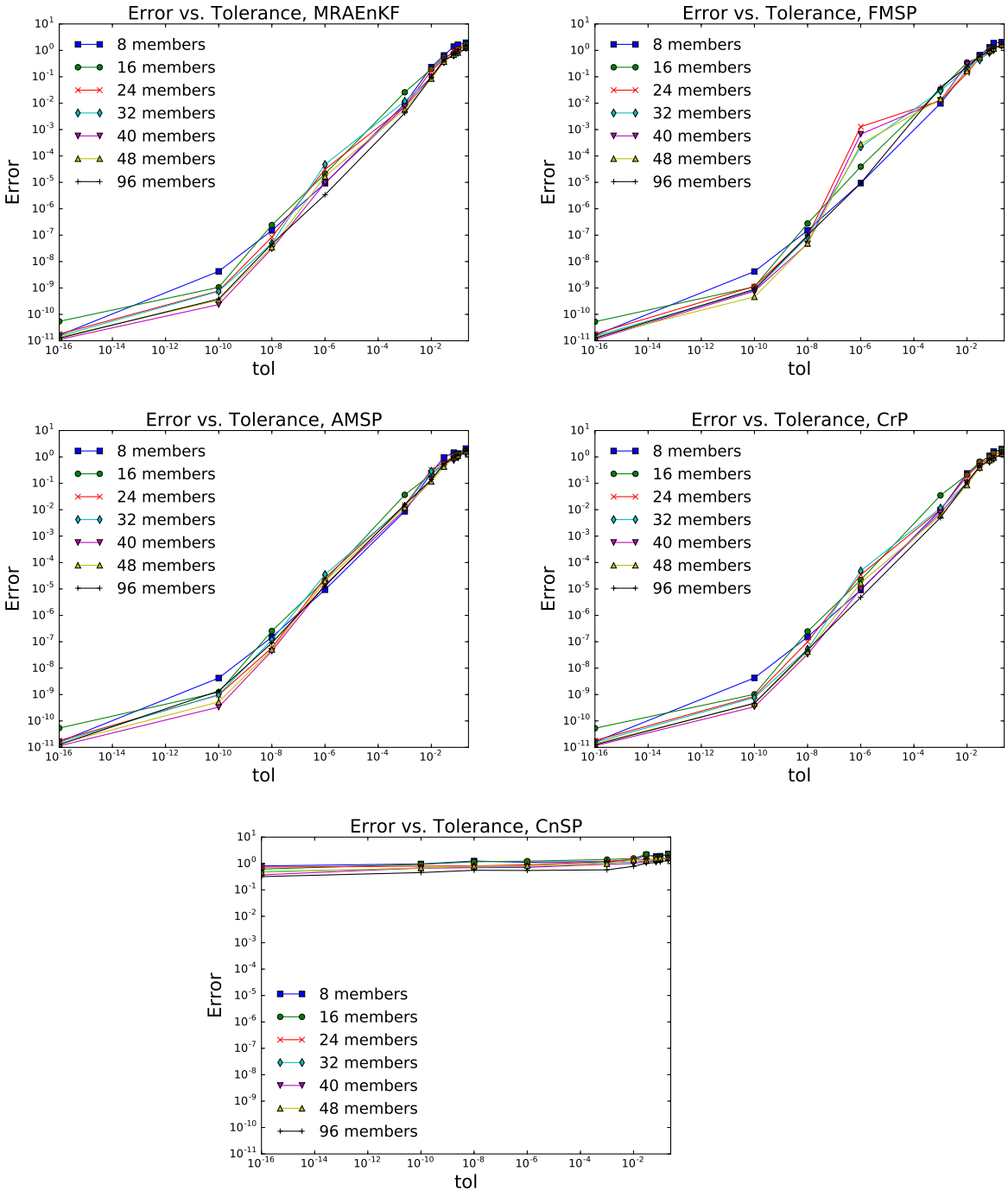

Figure 8: time-integrated RMSE versus tolerance. For each scheme, curves are generated for different ensemble size, as indicated.

6 Conclusions

We proposed a new framework combining a sequential data assimilation technique, namely the Ensemble Kalman Filter (EnKF), with adaptive mesh models. Specifically, a new class of adaptive mesh EnKF schemes has been developed, relying on a Multiresolution Analysis (MRA) approach to decompose the solution into Haar wavelets. A binary tree structure is used to index wavelet supports, which facilitates the implementation of coarsening and refinement operations. Based on user defined tolerances, the latter enable effective mesh adaptation of individual solutions represented by the ensemble members in the EnKF. Projections onto the wavelet spaces are incorporated into the EnKF update equation, which leads to the formulation of different MRA-EnKF schemes. By following different strategies for projecting and coarsening the ensemble members, and considering different ordering of projection and update operations, five different MRA-EnKF schemes were constructed. The first scheme, called "MRAEnKF" projects all members to the members union space for the EnKF update. The second scheme, FMSP, updates the members on the coarsened mean forecast space. The AMSP scheme (the counterpart of FMSP) updates the members on the coarsened mean analysis space (instead of the mean forecast space). The fourth proposed scheme, CrP, updates the members using FMSP first, then projects each member back onto the mesh of the previous forecast step. In the fifth scheme, CnSP, the analysis of each member is performed on the corresponding mesh, solely relying on the coarsening and refinement algorithms of the MRA.

These variants were evaluated against a fine-grid EnKF solution in a twin experiments setting involving the 1D Burger's equation. The analysis revealed that with an appropriate choice of tolerance, all MRA-EnKF methods accurately recovered the reference free-run solution except for CnSP, which poorly performed compared to the other schemes. This was not surprising because CnSP performs all operations in the space defined by each member. The numerical results also revealed that the other four methods accurately approximated the EnKF solution and lead to significant computational savings. Specifically, only marginal differences with the EnKF were obtained while computational complexity reductions of up to 50% were achieved relative to the reference fine grid solution.

These preliminary results also provide an insight into potential extensions of the proposed framework. Particularly, because with the same tolerance all methods led approximately to the same computational saving, one may select the preferred approach based on ease of implementation. In this regard, we found that for the same value of tolerance, the performance of MRAEnKF and CrP are similar for small ensembles. However, CrP requires several more projection steps to implement the algorithm. One may thus consider MRAEnKF as being a more convenient scheme.

The present work focused on an adaptive mesh formulation based on MRA and restricted our application to a one-dimensional setting. While the problem was a simple one, it was sufficiently involved in the sense that individual solution schemes led to substantially different grid adaptations and complexity to accuracy ratios. We expect our conclusions regarding the respective merits of the MRA-EnKF methods to be robust and to remain valid when applied to more elaborated settings in higher spatial dimensions with more complex models. More challenging problems should emphasize the differences between the methods and exhibit higher computational gains. Extension of the present constructions to multi-dimensional problems is in principle straightforward, particularly if one exploits generalizations of the presently used binary tree constructions, and coarsening/refinement operators (e.g. [49]). Though this would naturally involve more elaborate adaptive mesh algorithms, the computational savings achieved in multiple dimensions are generally anticipated to be much more substantial than in one space dimension. We finally note that our selection of the present mesh adaptation formalism was in large part based on the analytical capabilities of the used MRA approach. However, one should note that the developed adaptive mesh EnKF methodologies can be readily implemented with different discretization approaches and adaptation strategies. Again, our conclusions are expected to remain qualitatively valid when other adaptive approaches are employed for the advancement of the ensemble members, although the computational savings achieved may heavily depend on the selected approach.Besides the extension of general adaptive mesh algorithms, the application to large scale model may raise additional effects that were not active in our one-dimensional settings. A particular effect expected to emerge is the need of introducing localization in the ensemble

covariance, to prevent the emergence of spurious long-range interactions. In our opinion, the hierarchical nature of the MRA schemes presents new opportunities to develop scale-dependent localization strategies in the future, starting from the ideas proposed in [19]. In these situations, adaptive mesh strategies may not only reduce the computational complexity of the EnKF approaches but also improve their effectiveness by enabling better update procedures distinguishing the treatment of large and short scales. Such generalizations will be the subject of future studies.

Acknowledgement

This work was supported by the King Abdullah University of Science and Technology (KAUST) in Thuwal, Saudi Arabia, Collaborative Research Grant (CRG) program, grant number CRG3-2016.

References

[1] AIAA. *Guide for the Verification and Validation of Computational Fluid Dynamics Simulations (AIAA G-077-1998(2002))*, 1998.

[2] M. U. Altaf, T. Butler, T. Mayo, X. Luo, C. Dawson, A. W. Heemink, and I. Hoteit. A comparison of ensemble kalman filters for storm surge assimilation. *Monthly Weather Review*, 142(8):2899–2914, 2014.

[3] J.L. Anderson. An ensemble adjustment kalman filter for data assimilation. *Monthly Weather Review*, 129(12):2884–2903, 2001.

[4] Randolph E. Bank, Andrew H. Sherman, and Alan Weiser. Some refinement algorithms and data structures for regular local mesh refinement. In R. Stepleman et al., editor, *Scientfic Computing: Applications of Mathematics and Computing to the Physical Sciences*. IMACS/North-Holland, 1983.

[5] Marsha Berger and Phillip Colella. Local adaptive mesh refinement for shock hydrodynamics. *Journal of Computational Physics*, 82:64–84, 05 1989.

[6] Marsha J. Berger, David L. George, Randall J. LeVeque, and Kyle T. Mandli. The geoclaw software for depth-averaged flows with adaptive refinement. *Advances in Water Resources*, 34(9):1195 – 1206, 2011.

[7] Marsha J Berger and Joseph Oliger. Adaptive mesh refinement for hyperbolic partial differential equations. *Journal of Computational Physics*, 53(3):484 – 512, 1984.

[8] Craig H. Bishop, Brian J. Etherton, and Sharanya J. Majumdar. Adaptive sampling with the ensemble transform kalman filter. part i: Theoretical aspects. *Monthly Weather Review*, 129(3):420–436, 2015/11/02 2001.

[9] Gerrit Burgers, Peter Jan van Leeuwen, and Geir Evensen. Analysis scheme in the ensemble kalman filter. *Monthly Weather Review*, 126(6):1719–1724, 1998.

[10] Carsten Burstedde, Lucas C. Wilcox, and Omar Ghattas. p4est: Scalable algorithms for parallel adaptive mesh refinement on forests of octrees. *SIAM Journal on Scientific Computing*, 33(3):1103–1133, 2011.

[11] M. D. Butala, R. A. Frazin, Y. Chen, and F. Kamalabadi. Tomographic imaging of dynamic objects with the ensemble kalman filter. *IEEE Transactions on Image Processing*, 18(7):1573–1587, July 2009.

[12] T Butler, MU Altaf, C Dawson, Ibrahim Hoteit, X Luo, and T Mayo. Data assimilation within the advanced circulation (adcirc) modeling framework for hurricane storm surge forecasting. *Monthly Weather Review*, 140(7):2215–2231, 2012.

[13] C. Dawson and R. Kirby. High resolution schemes for conservation laws with locally varying time steps. *SIAM Journal on Scientific Computing*, 22(6):2256–2281, 2001.

[14] Juan Du, Jiang Zhu, Fangxin Fang, C. C. Pain, and I. M. Navon. Ensemble data assimilation applied to an adaptive mesh ocean model. *International Journal for Numerical Methods in Fluids*, 82(12):997–1009, 2016.

[15] Geir Evensen. The ensemble kalman filter: theoretical formulation and practical implementation. *Ocean Dynamics*, 53(4):343–367, Nov 2003.

[16] F. Fang, C. C. Pain, I. M. Navon, M. D. Piggott, G. J. Gorman, P. E. Farrell, P. A. Allison, and A. J. H. Goddard. A pod reduced-order 4d-var adaptive mesh ocean modelling approach. *International Journal for Numerical Methods in Fluids*, 60(7):709–732, 2009.

[17] K. Fossum and T. Mannseth. Coarse-scale data assimilation as a generic alternative to localization. *Comput. Geosci.*, 21:167–186, 2017.

[18] D. Gamerman and H. Lopes. *Markov Chain Monte Carlo: Stochastic Simulation for Bayesian Inference*. Chapman and Hall/CRC, Boca Raton, 2006.

[19] T. Gentilhomme, D.S. Oliver, T. Mannseth, G. Caumon, R. Moyen, and P. Doyen. Ensemble-based multi-scale history-matching using second-generation wavelet transform. *Comput. Geosci.*, 19:999–1025, 2015.

[20] Loïc Giraldi, Olivier P. Le Maître, Kyle T. Mandli, Clint N. Dawson, Ibrahim Hoteit, and Omar M. Knio. Bayesian inference of earthquake parameters from buoy data using a polynomial chaos-based surrogate. *Computational Geosciences*, 21(4):683–699, Aug 2017.

[21] Jinlan Gou, Xin Yuan, and Xinrong Su. Adaptive mesh refinement method based investigation of the interaction between shock wave, boundary layer, and tip vortex in a transonic compressor. *Proceedings of the Institution of Mechanical Engineers, Part G: Journal of Aerospace Engineering*, 232(4):694–715, 2018.

[22] Dilshad Haleem, Georges Kesserwani, and Daniel Caviedes-Voullième. Haar wavelet-based adaptive finite volume shallow water solver. *Journal of Hydroinformatics*, 17:6, 07 2015.

[23] Ami Harten. Multiresolution algorithms for the numerical solution of hyperbolic conservation laws. *Communications on Pure and Applied Mathematics*, 48(12):1305–1342, 1995.

[24] W. K. Hastings. Monte carlo sampling methods using markov chains and their applications. *Biometrika*, 57(1):97–109, 1970.

[25] I. Hoteit, D.-T. Pham, M. E. Gharamti, and X. Luo. Mitigating observation perturbation sampling errors in the stochastic enkf. *Monthly Weather Review*, 143(7):2918–2936, 2015.

[26] I. Hoteit, D-T. Pham, G. Triantafyllou, and G. Korres. A new approximate solution of the optimal nonlinear filter for data assimilation in meteorology and oceanography. *Monthly Weather Review*, 136(1):317–334, 2008.

[27] Ibrahim Hoteit, Tim Hoar, Ganesh Gopalakrishnan, Nancy Collins, Jeffrey Anderson, Bruce Cornuelle, Armin Köhl, and Patrick Heimbach. A mitgcm/dart ensemble analysis and prediction system with application to the gulf of mexico. *Dynamics of Atmospheres and Oceans*, 63:1 – 23, 2013.

[28] Ibrahim Hoteit, Xiaodong Luo, and Dinh-Tuan Pham. Particle kalman filtering: A nonlinear bayesian framework for ensemble kalman filters. *Monthly Weather Review*, 140(2):528–542, 2012.

[29] Ibrahim Hoteit, Dinh-Tuan Pham, and Jacques Blum. A simplified reduced order kalman filtering and application to altimetric data assimilation in tropical pacific. *Journal of Marine Systems*, 36(1–2):101 – 127, 2002.

[30] Pushkar Kumar Jain, Kyle Mandli, Ibrahim Hoteit, Omar Knio, and Clint Dawson. Dynamically adaptive data-driven simulation of extreme hydrological flows. *Ocean Modelling*, 122:85 – 103, 2018.

[31] Rudolf Kalman. A new approach to linear filtering and prediction problems. *Transactions of the ASME - Journal of Basic Engineering*, 82:35–45, 01 1960.

[32] Noboru Kikuchi. Adaptive grid-design methods for finite element analysis. *Computer Methods in Applied Mechanics and Engineering*, 55(1):129 – 160, 1986.

[33] G. Korres, G. Triantafyllou, G. Petihakis, D.E. Raitsos, I. Hoteit, A. Pollani, S. Colella, and K. Tsiaras. A data assimilation tool for the pagasitikos gulf ecosystem dynamics: Methods and benefits. *Journal of Marine Systems*, 94:S102 – S117, 2012.

[34] Jan Mandel, Loren Cobb, and Jonathan D. Beezley. On the convergence of the ensemble kalman filter. *Applications of Mathematics*, 56(6):533–541, Dec 2011.

[35] Kyle T. Mandli, Aron J. Ahmadia, Marsha Berger, Donna Calhoun, David L. George, Yiannis Hadjimichael, David I. Ketcheson, Grady I. Lemoine, and Randall J. LeVeque. Clawpack: building an open source ecosystem for solving hyperbolic pdes. *PeerJ Computer Science*, 2:e68, August 2016.

[36] Kyle T. Mandli and Clint N. Dawson. Adaptive mesh refinement for storm surge. *Ocean Modelling*, 75:36 – 50, 2014.

[37] Per Pettersson, Gianluca Iaccarino, and Jan Nordström. Numerical analysis of the burgers' equation in the presence of uncertainty. *Journal of Computational Physics*, 228(22):8394 – 8412, 2009.

[38] Chiara Piccolo and Mike Cullen. A new implementation of the adaptive mesh transform in the met office 3d-var system. *Quarterly Journal of the Royal Meteorological Society*, 138(667):1560–1570, 2012.

[39] Derek J. Posselt and Craig H. Bishop. Nonlinear parameter estimation: Comparison of an ensemble kalman smoother with a markov chain monte carlo algorithm. *Monthly Weather Review*, 140(6):1957–1974, 2012.

[40] G. Y. H. El Serafy and A. E. Mynett. Improving the operational forecasting system of the stratified flow in osaka bay using an ensemble kalman filter-based steady state kalman filter. *Water Resource Research*, 44, 2008.

[41] Adil Siripatana, Talea Mayo, Omar Knio, Clint Dawson, Olivier Le Maître, and Ibrahim Hoteit. Ensemble kalman filter inference of spatially-varying manning's n coefficients in the coastal ocean. *Journal of Hydrology*, 562:664 – 684, 2018.

[42] Adil Siripatana, Talea Mayo, Ihab Sraj, Omar Knio, Clint Dawson, Olivier Le Maitre, and Ibrahim Hoteit. Assessing an ensemble kalman filter inference of manning's n coefficient of an idealized tidal inlet against a polynomial chaos-based mcmc. *Ocean Dynamics*, 67(8):1067–1094, Aug 2017.

[43] Ihab Sraj, KyleT Mandli, OmarM Knio, ClintN Dawson, and Ibrahim Hoteit. Uncertainty quantification and inference of manning's friction coefficients using dart buoy data during the tōhoku tsunami. *Ocean Modelling*, 83:82–97, 2014.

[44] Ihab Sraj, Olivier P. Le Maître, Omar M. Knio, and Ibrahim Hoteit. Coordinate transformation and polynomial chaos for the bayesian inference of a gaussian process with parametrized prior covariance function. *Computer Methods in Applied Mechanics and Engineering*, 298:205 – 228, 2016.

[45] W. Sweldens. The lifting scheme: A construction of second generation wavelets. *SIAM J. Math. Anal.*, 29:511–546, 1998.

[46] Albert Tarantola. *Inverse Problem Theory and Methods for Model Parameter Estimation*. Society for Industrial and Applied Mathematics, Philadelphia, PA, USA, 2004.

[47] Michael K. Tippett, Jeffrey L. Anderson, Craig H. Bishop, Thomas M. Hamill, and Jeffrey S. Whitaker. Ensemble square root filters. *Monthly Weather Review*, 131(7):1485–1490, 2003.

[48] Eleuterio F. Toro. *Riemann solvers and numerical methods for fluid dynamics: A practical introduction*. Springer-Verlag, Berlin, second edition, 1999.

[49] J. Tryoen, O. Le Maitre, and A. Ern. Adaptive anisotropic spectral stochastic methods for uncertain scalar conservation laws. *SIAM Journal on Scientific Computing*, 34(5):A2459–A2481, 2012.